JOURNAL OF SYNCHROTRON RADIATION
ISSN 1600-5775

X-ray reflectivity from curved liquid interfaces

Sven Festersen,[a] Stjepan B. Hrkac,[a] Christian T. Koops,[a] Benjamin Runge,[a] Thomas Dane,[b] Bridget M. Murphy[a,c]* and Olaf M. Magnussen[a,c]

[a]Institute for Experimental and Applied Physics, Kiel University, Kiel, Germany, [b]ESRF, The European Synchrotron, 71 Avenue des Martyrs, 38000 Grenoble, France, and [c]Ruprecht-Haensel-Laboratory, Kiel University, Kiel, Germany. *Correspondence e-mail: murphy@physik.uni-kiel.de

Received 28 July 2017
Accepted 18 December 2017

Edited by G. Grübel, HASYLAB at DESY, Germany

Keywords: X-ray reflectivity; liquid interfaces; methods; free-elecron laser; synchrotron.

X-ray reflectivity studies of the structure of liquid–vapour and liquid–liquid interfaces at modern sources, such as free-electron lasers, are currently impeded by the lack of dedicated liquid surface diffractometers. It is shown that this obstacle can be overcome by an alternative experimental approach that uses the natural curvature of a liquid drop for variation of the angle of incidence. Two modes of operation are shown: (i) sequential reflectivity measurements by a nanometre beam and (ii) parallel acquisition of large ranges of a reflectivity curve by micrometre beams. The feasibility of the two methods is demonstrated by studies of the Hg/vapour, H_2O/vapour and Hg/0.1 *M* NaF interface. The obtained reflectivity curves match the data obtained by conventional techniques up to $5\alpha_c$ in micro-beam mode and up to $35\alpha_c$ in nano-beam mode, allowing observation of the Hg layering peak.

1. Introduction

X-ray reflectivity (XRR) techniques enable structural studies with molecular resolution on the electron-density profiles along interface normals (Als-Nielsen & McMorrow, 2011; Seeck & Murphy, 2015). Their application on liquid/liquid systems is of particular interest as such systems play a major role in biological systems and provide opportunities for technical applications. Conventional XRR methods require both an extended flat fluidic interface and the means to change the angle of the incident X-ray beam. At synchrotron X-ray sources, beam tilting is currently achieved by highly specialized liquid surface diffractometers. Available instrument designs employ either Bragg reflection at one (Als-Nielsen & Pershan, 1983; Schlossman *et al.*, 1997) or at two subsequent crystals (Honkimäki *et al.*, 2006; Murphy *et al.*, 2014; Seeck & Murphy, 2015) for tilting the beam down on the liquid surface. However, these setups and others outlined by Pershan & Schlossman (2012) are available at only a few synchrotron beamlines worldwide and do not exist at all at current or upcoming free-electron laser (FEL) sources, limiting the application of XRR methods to liquid interfaces. Alternative techniques such as angular-dispersive (Naudon *et al.*, 1989) and energy-dispersive (Metzger *et al.*, 1994; Pietsch *et al.*, 2001) XRR allow a fixed setup, but necessitate specialized optics and energy-sensitive detectors.

Here, we present a method that circumvents the experimental challenges by utilizing the curved surface of a liquid drop to reflect an X-ray beam impinging horizontally. If a sessile drop is used in combination with a narrow beam (of the order of 100 nm high), the surface curvature enables reflection angles from 0 to 180°, selected by a simple vertical translation of the drop relative to the beam. Use of a broader (of the

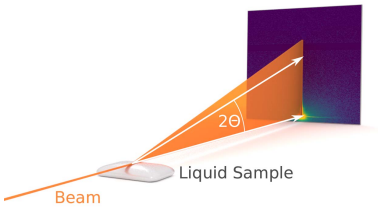

OPEN ACCESS

order of 10 µm) beam gives access to a large range of the reflectivity curve in one measurement, thus enabling fast acquisition for low reflection angles similar to the RAPID XRR (Yano *et al.*, 2009) method. The sole experimental prerequisites for both modes are a vertical translation stage for the sample, a two-dimensional detector and the ability to vertically focus the X-ray beam down to the required height at the sample. These requirements are nowadays met at most modern synchrotron and FEL beamlines.

Extended discussions of the influence of the interface curvature on the reflected beam and the difficulties arising exist for solid/liquid (Briscoe *et al.*, 2012) and liquid/vapour interfaces (Kawamoto *et al.*, 1993; Regan *et al.*, 1997). The application of the broad-beam geometry as a useful method was proposed by Bosio *et al.* in 1989 (Bosio *et al.*, 1989), but abandoned due to experimental difficulties at that time.

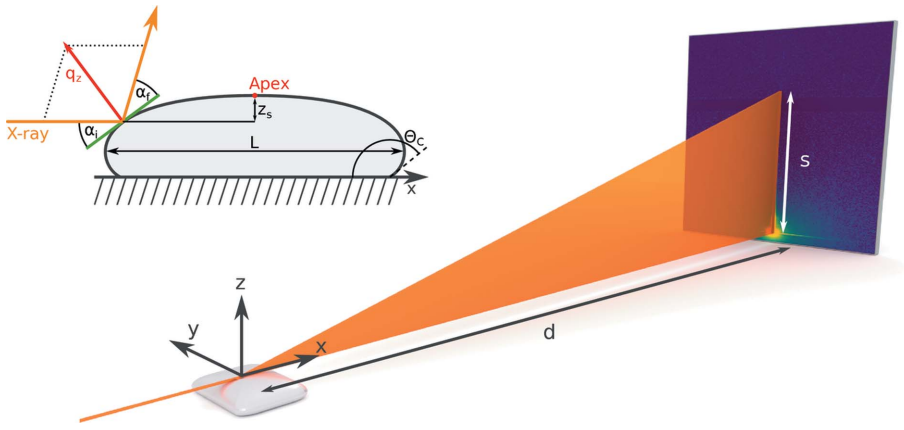

Figure 1
Sketch of the proposed reflection geometry. A horizontal X-ray beam (along the x direction) is reflected from the surface of a liquid drop and detected by a two-dimensional detector. Incident angle α_i and reflection angle α_f depend solely on the local curvature.

We demonstrate the feasibility of this reflection geometry on a polar liquid (water), a liquid metal (mercury), and the interface between a liquid metal and an aqueous electrolyte solution. Specifically, the nano-beam mode was used to record the XRR curve of the mercury/vapour interface, while the micro-beam mode was used to record the XRR curves of the water/vapour interface, the mercury/vapour interface and the mercury/electrolyte interface. These samples were chosen because of their high surface tension and high X-ray reflectance, which results in intense and sharp reflections. In addition, liquid metals such as mercury exhibit a strong stratification of the atomic layers close to the interface, resulting in a pseudo-Bragg peak (*layering peak*) at $q_z = 2/(3^{1/2}r)$, where r is the atomic radius (Magnussen *et al.*, 1995; Dimasi & Tostmann, 1999). For mercury, the peak is located at $q_z \simeq 2.2$ Å^{-1}. Here, we pay special attention to the layering peak's visibility as an indicator for the reflectivity method's performance. A high-brilliance synchrotron beam is required as the layering peak intensity is not only six to seven orders of magnitude lower than the incident-beam's intensity, but is also superimposed on the liquid scattering peak.

2. Principle of measurement

We consider a sessile drop placed on the x/y plane centred around the z axis. The angle between the x/y plane and a local tangent to the surface then varies from 0° at the drop's apex to the contact angle Θ_C at its base (see Fig. 1 inset). A horizontal ray with negligible width and height travelling parallel to the x axis and impinging on the drop's surface is reflected at the local tangent plane. For drops that are symmetrical with respect to the x/z plane, the reflected ray is located in that plane. The angle of reflection measured relative to the x/y plane depends on the vertical position of the impingement point. The following discussion is restricted to the case of a drop with negligible curvature in the x/y plane and a ray impinging perpendicular to the drop's edge. This can be experimentally achieved by a very large puddle or confinement of the drop inside a rectangular container. If a highly collimated beam with finite height and width is used instead of a point-like ray, the reflection from the drop is spread over an angular range (see Fig. 1) which depends on the height of the beam, the drop's shape and the vertical position of the impingement point on the drop. We now derive the relationship between the vertical position z_s of a ray with respect to the drop's apex and the reflection angle. Since a universal expression for the shape of a drop does not exist, we assume a semi-infinite puddle with its edge at $x = 0$. It can then be shown that for non-wetting systems ($\Theta_C > 90°$) the angle between the local tangent and the horizontal α_i is given by (Adamson & Gast, 1997; de Gennes *et al.*, 2004)

$$\alpha_i(z_s) = \arctan\left(\frac{dz_s}{dx}\right) = \arctan\left[\left(1 - \frac{z_s^2}{\Lambda_c^2}\right)^{-2} - 1\right]^{1/2} \quad (1)$$

where $\Lambda_c = (\gamma/\rho g)^{1/2}$ is the capillary length of the liquid given by its surface tension γ, the liquid's density ρ and the gravitational acceleration g. For small incident angles, equation (1) can be approximated by a linear expression,

$$\alpha_i(z_s) \simeq 2^{1/2}\frac{z_s}{\Lambda_c}. \quad (2)$$

This approximation deviates by less than 0.55% from the exact solution for $\alpha_i < 10°$. A ray impinging on the drop is reflected by $\alpha_i + \alpha_f = 2\alpha_i$. Consequently, a perfectly collimated beam with finite height h is spread over an angular range of

$$\Delta(\alpha_i + \alpha_f) \simeq 2(2)^{1/2}\frac{h}{\Lambda_c}, \quad (3)$$

corresponding to a range of wavevector transfer values of approximately

$$\Delta q_z \simeq \frac{4\pi}{\lambda} 2^{1/2} \frac{h}{\Lambda_c}. \quad (4)$$

In the following paragraph, we will discuss the effect of vertical divergence (in the x/z plane) and horizontal divergence (in the x/y plane) on the reflection. Divergence Θ_D in the vertical direction leads to a distribution of incident angles around α_i with width Θ_C. If a collimated beam is spread into an angular range $\Delta(\alpha_i + \alpha_f)$, the divergent beam is spread into the range $\Delta(\alpha_i + \alpha_f) + \Theta_D$. The vertical divergence thus effectively increases the angular range covered by the beam, but lowers the q_z resolution to

$$\Delta q_z = \left|\frac{2\pi}{\lambda} \cos(\alpha_i)\right| \Theta_D, \quad (5)$$

which is most relevant at small angles. Let us now consider the horizontal divergence Θ_D only. While the angle between the local tangent and a non-divergent beam would be α_i, the effective angle α_{eff} in the divergent case (Fig. 2*a*) can be calculated given the vector of an incoming ray $\mathbf{r} = (\cos\Theta_D, \sin\Theta_D, 0)$ and the tangent plane's normal vector $\mathbf{n} = (\sin\alpha_i, 0, \cos\alpha_i)$,

$$\begin{aligned} \alpha_{eff} &= 90^\circ - \arccos(\mathbf{n}\cdot\mathbf{r}) \\ &= 90^\circ - \arccos\left[\sin(\alpha_i)\cos(\Theta_D)\right], \end{aligned} \quad (6)$$

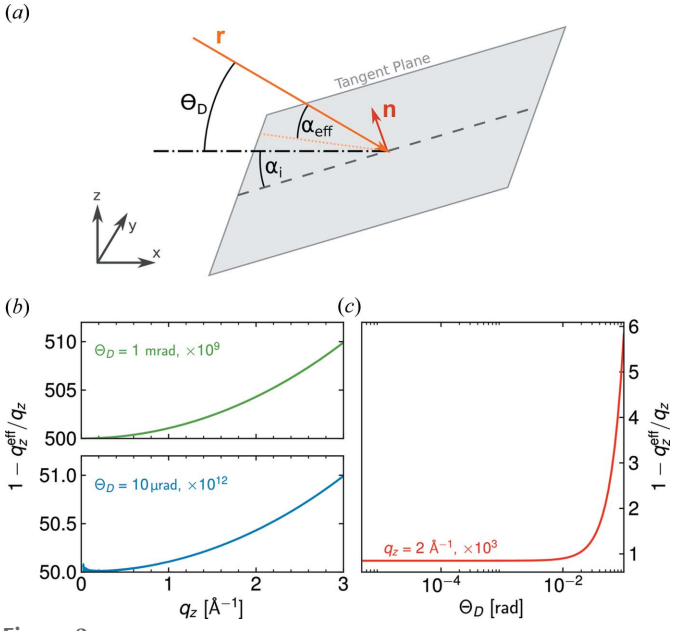

Figure 2
Horizontal divergence. (*a*) Because of the angle between the horizontal (dash–dotted line) and a ray of a beam (orange) with non-zero horizontal divergence Θ_D, the incident angle is effectively lowered from α_i to α_{eff}. The effective angle can be calculated from the ray vector **r** and the tangent plane normal **n**. (*b*) Deviation of q_z^{eff} from q_z for two different horizontal divergence values. The effect is most pronounced for large q_z. (*c*) Deviation of q_z^{eff} from q_z depending on divergence for a relatively high value of $q_z = 2$ Å^{-1}.

which effectively lowers the incident angle and consequently the effective momentum transfer q_z^{eff}. Fig. 2(*b*) shows the relative deviation of q_z^{eff} from q_z for divergence values of 10 µrad (Seeck *et al.*, 2012) (blue) and 1 mrad (Riekel *et al.*, 2010) (green). Even for high angles ≥ 2 Å^{-1} and a divergence of 1 mrad, the relative deviation is below 10^{-6}. Fig. 2(*c*) shows the relative deviation of the effective momentum transfer from q_z for a momentum transfer of 2 Å^{-1} over a wide range of divergence values. The deviation is negligible for divergence values $\leq 10^{-2}$ rad. These considerations show that divergence effects are negligible at undulator beamlines of modern synchrotron sources.

To utilize this geometry for XRR measurements with a horizontal X-ray beam (wavelength λ), the droplet has to be placed on a vertical translation stage to change the reflection angle by variation of z_s. A two-dimensional detector, placed at a distance d from the impingement point (Fig. 1), is required for measuring the reflected beam as well as the background. The reflection angle can be calculated from the vertical position s of the reflected beam on the detector relative to the primary beam position *via* $\alpha_i + \alpha_f = \arctan(s/d)$ (Fig. 1). From this, the surface normal momentum transfer is easily calculated as $q_z = (4\pi/\lambda)\sin[(\alpha_i + \alpha_f)/2]$. It should be noted that the position of the impingement point in the horizontal direction (along the primary beam) changes with z_s as the point moves along the surface. With a fixed detector, this leads to an error in d of $\Delta d \leq L/2$, where L is the size of the droplet in the horizontal direction. The observed beam position on the detector s therefore is systematically shifted by $\Delta s/s = \Delta d/d \leq L/(2d)$. Δs can thus be minimized by increasing the detector–sample distance and reducing the size of the drop. To correct for this shift, it is necessary to know the inverse of the function describing the shape of the drop, $x(z_s)$. Even for the simple case of a semi-infinite sample, this is not possible analytically (de Gennes *et al.*, 2004) and will not be discussed here. However, near the apex the differential equation $(dz_s)/(dx) = \tan\alpha_i \simeq 2^{1/2}(z_s - a)/\Lambda_c$ can be solved within the linear approximations [equations (3) and (4)]. The resulting offset in q_z can then be estimated for a drop with contact angle Θ_C as

$$\Delta q_z^{off} \simeq \left|\frac{4\pi}{\lambda}\right| \left|\frac{s}{d^2 + s^2}\right| \frac{\Lambda_c}{2^{1/2}} \ln\left(\frac{\Lambda_c}{2^{1/2}a}\tan\alpha_i + 1\right), \quad (7)$$

where $a = 2\Lambda_c \sin(\Theta_C/2)$ is the height of the sessile drop. At typical X-ray wavelengths, *e.g.* 1 Å, Δq_z^{off} is $\leq 10^{-6}$ Å^{-1} for the mercury/vapour interface and the water/vapour interface at q_z positions close to the critical angle and therefore negligible. Even though Δq_z^{off} increases with q_z, it does not exceed 3×10^{-3} Å^{-1} at $q_z > 2.0$ Å^{-1} for both systems.

A beam with a height h of the order of 10 to 100 µm can be utilized to probe a large range of the XRR curve with a single detector image. We will refer to this mode of operation as *micro-beam mode* throughout this paper. Because the primary beam in this case is scattered into a range of q_z values, the intensity at each q_z is lower compared with conventional XRR methods, leading to worse counting statistics. This is particularly problematic if diffuse scattering from the surface or

Table 1
In micro-beam mode, angular resolution $\Delta(\alpha_i + \alpha_f)$ and momentum transfer resolution Δq_z depend on detector pixel size and distance between sample and detector.

Pixel size (μm)	d (m)	$\Delta(\alpha_i + \alpha_f)$ (°)	Δq_z (λ = 1 Å, q_z = 0) (Å^{-1})
50	0.3	0.019	0.0021
50	1.2	0.005	0.0005
172	1.4	0.014	0.0015

scattering from the liquid bulk become comparable with the specular intensity (Braslau *et al.*, 1988). For liquid surfaces, the diffuse scattering and the reflectivity are inherently correlated. Separation of these components requires complex mathematical models (Shpyrko *et al.*, 2003; Runge *et al.*, 2016) that take the beam profile and drop shape into account and are beyond the scope of this paper. For the systems studied here, no increased intensity due to diffuse scattering was experimentally observed (see below). The micro-beam mode is thus limited to low q_z values where the reflected intensity is at least an order of magnitude higher than those of other scattering contributions.

In this mode, the q_z resolution is determined by the detector pixel size and the detector's distance from the sample. Table 1 lists the calculated resolution for three combinations of pixel size and detector distance used in the experiments described in this paper. The table shows that these parameters have to be chosen carefully to obtain sufficient resolution at low angles. At a wavelength of λ = 1 Å, a detector with 50 μm pixel size placed at a distance of 1.2 m from the sample allows a resolution of 0.0005 Å^{-1}, sufficiently small to resolve the critical angle of, for example, water (0.0217 Å^{-1}).

Micro-beam mode requires a highly collimated beam, otherwise the recorded intensity is convoluted with the angular distribution. Furthermore, the intensity depends on the vertical beam profile. To obtain a constant scaling factor, a flat-top beam profile is preferred for this mode.

For a small vertical beam size h of the order of nanometres, the spreading of the reflected beam $\Delta(\alpha_i + \alpha_f)$ and Δq_z becomes small enough to resolve the critical angle of the studied liquids at typical X-ray wavelengths. Assuming a beam with $h \leq 200$ nm and $\lambda = 1$ Å, equation (4) yields $\Delta q_z \leq 0.0013$ Å^{-1} for the water/vapour and $\Delta q_z \leq 0.0019$ Å^{-1} for the mercury/vapour interface. Both values are considerably smaller than the respective critical angles. By translation of the sample in the vertical direction, the XRR curve can be recorded step by step, similar to classical techniques. In practice, a beam with $h \simeq 100$ nm is sufficiently small to apply this technique. We will therefore refer to this mode of operation as *nano-beam mode*. Assuming a beam of height h with a flat-top profile, the Fresnel reflectivity R_F within the measured q_z range Δq_z given by equation (4) is largest near the critical angle, with variations of up to 15% for the mercury/vapour interface. This variation biases the measured q_z to lower values at q_z positions where the reflectivity exhibits strong variations. For a beam with $h = 170$ nm and $\lambda = 1$ Å, the deviation of q_z observed on the mercury/vapour interface is below 3% at the critical angle. The bias can be reduced further by using a beam with a Gaussian profile. Further uncertainties in the q_z position arise from the vertical beam divergence Θ_D as described by equation (5).

3. Experimental details

Measurements in nano-beam mode were carried out at the nanofocus endstation of ESRF beamline ID13, which provides a vertical beam size of 170 nm at an energy of 15.2 keV and a vertical divergence in the order of 1 mrad (Riekel *et al.*, 2010). These experiments were performed on clean mercury surfaces in N_2 (purity N5.7) atmosphere [Λ_c = 1.91 mm (Adamson & Gast, 1997; Dean & Lange, 1999), drop height a = 3.71 mm]. Equation (5) yields a $\Delta q_z/q_z$ of 12.5% at the critical angle due to the high beam divergence, dropping to 7% at $q_z = 0.1$ Å^{-1} and becoming less than 1% above $q_z = 0.7$ Å^{-1}. Instead of a free sessile drop, we used Hg samples contained in a purpose-built KEL-F cell of rectangular shape (1.0 × 0.8 cm, beam impinging on the long edge) to ensure reproducible drop size and orientation. A two-dimensional detector (Dectris Ltd, Eiger 4M, 75 × 75 μm pixel size, distance d = 0.3 m) was used for data acquisition. XRR curves were recorded up to the liquid metal layering peak at approximately 2.2 Å^{-1}, corresponding to $\alpha_i + \alpha_f = 16.42°$ at the given photon energy. Starting with the incoming beam half-shaded by the sample, the vertical sample position was changed stepwise and a single detector image was recorded for each point of the XRR curve. The detector images were monitor-normalized and corrected by subtraction of the background intensity measured 15 pixels left and right of the specular reflection. The specular intensity was extracted by integration of a 12 × 150 pixel area. The reflection's vertical position s on the detector was obtained by a Gaussian fit to the vertical profile of the same area, then mapped to an angle α_i and converted to a momentum transfer value q_z. Measurements were carried out on two mercury samples prepared under identical conditions. XRR data were recorded for $q_z > 1.3$ Å^{-1} on the first sample and for $q_z < 1.2$ Å^{-1} on the second sample with exposure times from 1 to 240 s per step.

The micro-beam mode was used to record XRR curves of the water/vapour interface [in air, Λ_c = 2.71 mm (Adamson & Gast, 1997; Dean & Lange, 1999)] at a photon energy of 15 keV using a beam of 100 μm vertical size and a Dectris Ltd Eiger 1M detector (75 × 75 μm pixel size, distance d = 1.196 m) with total exposure times of 1–100 s. Identical energy and beam size were used to record XRR curves of the mercury/vapour interface (in N_2 atmosphere) with a Dectris Ltd Pilatus 100k detector (172 × 172 μm pixel size, distance d = 1.394 m) and a total exposure time of 1 s. The XRR curves of the mercury/electrolyte interface (in N_2 atmosphere) were recorded at an energy of 25 keV using a Dectris Ltd Eiger 1M detector (distance d = 1.22 m) with 1 s total exposure time. The water sample was contained in a sample cell with a rectangular shape (4.0 × 19.5 cm, PTFE), mercury samples were contained in circular sample cells (diameter 4 cm, KEL-F). The recorded two-dimensional data sets were integrated in

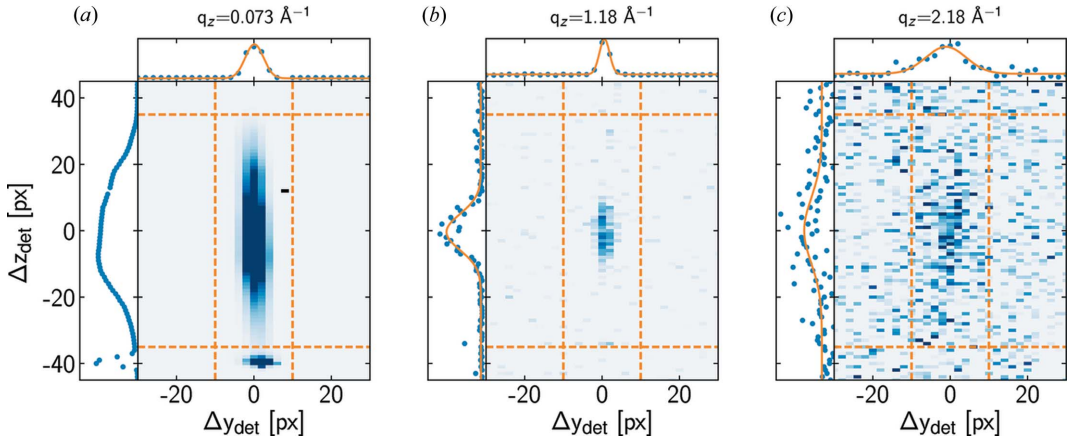

Figure 3
Reflected intensity (background-corrected) recorded in nano-beam mode at three different q_z values. The dashed orange lines denote the area from which the y_{det} and z_{det} profiles were obtained by integration in vertical and horizontal directions. The intensity profiles were fitted by Gaussians (solid orange lines) to determine the reflection peak positions. Exposure times were (*a*) 10 s, (*b*) 240 s and (*c*) 480 s.

the horizontal direction (ten pixels wide for water/vapour and mercury/electrolyte and five pixels wide for mercury/vapour to obtain similar integration regions with different detector pixel size) and the vertical pixel coordinates were mapped to q_z values. All micro-beam experiments were carried out at room temperature using the sample and detector stage of the LISA liquid diffractometer (Murphy *et al.*, 2014) at the PETRA III high-resolution diffraction beamline P08, where the vertical divergence does not exceed 10 µrad in collimation mode (Seeck *et al.*, 2012). The vertical spread of the beam due to the divergence is below the size of two detector pixels and is therefore neglected. The sufficiently large incoming beam was cut by a vertical slit system to obtain a quasi-flat-top beam profile.

At both sources, Gaussian beam profiles were confirmed by knife-edge scans and slit settings were optimized to avoid slit diffraction. All sample cell parts that came in contact with the sample liquids were cleaned in a mixture of H_2SO_4 and H_2O_2 (water/vapour and mercury/electrolyte experiments) or HNO_3 (mercury/vapour experiments) to avoid contamination of the interface and ensure cleanliness of the sample cell. Milli-Q water was used for the water/vapour sample and to prepare the 0.1 *M* NaF (99.995%, Alfa Aesar) aqueous solution for the mercury/electrolyte sample. High-purity mercury (99.99+%, Chempur) was used in all studies of the mercury interface.

4. Results and discussion

Examples of reflections from the mercury/vapour interface recorded in nano-beam mode are shown in Fig. 3. The presented images were recorded at q_z = 0.073, 1.18 and 2.18 Å^{-1} and are background-corrected. The data shown in Fig. 3(*a*) (exposure time 10 s) include a part of the primary beam that is transmitted over the sample due to the very small vertical translation (visible at the bottom of the plot). As the sample is further translated upwards, the primary beam intensity is completely cut off by the sample. Data recorded at q_z = 1.18 Å^{-1} (Fig. 3*b*) exhibit the expected Gaussian-shaped reflection. The reflection shown in Fig. 3(*c*) was recorded at the mercury layering peak position. The intensity at this position is expected to be a factor of approximately 10^{-7} reduced compared with the primary beam intensity. Still, a distinct peak was observed with an exposure time of 480 s.

Fig. 4 shows the XRR curves of the first (green triangles) and the second mercury sample (blue circles). The observed integrated intensity below the critical angle was 10^5 counts s^{-1}. Compared with the Fresnel reflectivity of a perfectly sharp interface (dotted black line), the data measured on the first sample exhibit the expected maximum at 2.2 Å^{-1}, arising from the stratification of the near-surface Hg into atomic layers. The data are in good agreement with previous studies of the free liquid Hg surface at room temperature, measured in conventional geometry on liquid surface diffractometers (Magnussen *et al.*, 1995). Fits of the distorted crystal model (DCM), which

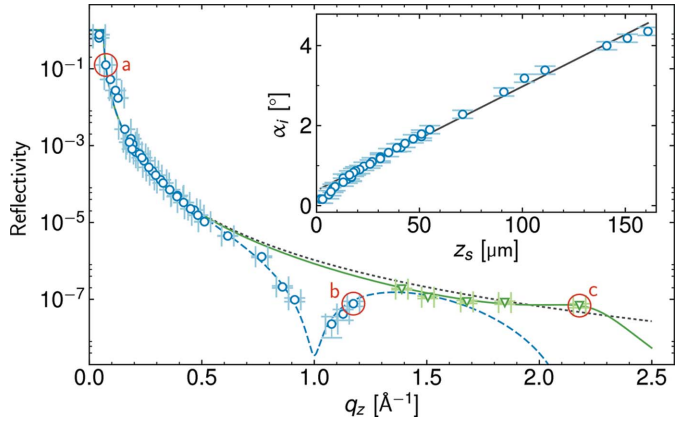

Figure 4
XRR curves of the mercury/vapour interface measured on two samples using a 170 nm beam. Data on the first sample (green triangles) exhibit the characteristic layering peak and are in good agreement with literature values (Magnussen *et al.*, 1995). Oscillations in the XRR curve of the second sample (blue circles) suggest a mercury oxide layer at the interface. The dotted black line indicates the Fresnel reflectivity. Inset: incident angle *versus* sample translation measured on the second sample (blue circles) with fit of equation (1) (black line).

is commonly used to describe the liquid metal layering (solid green line), with a fixed layer spacing of 2.76 Å yielded an intrinsic roughness of (0.982±0.013) Å and layer broadening of (0.459±0.027) Å, which are in good agreement with the values reported previously. Data measured at low angles on the second sample revealed a distinct intensity minimum at 1 $Å^{-1}$, indicating an additional layer at the interface. A fit of a DCM modified by an adlayer (dashed blue line) yields a layer thickness of (5.82±0.42) Å, which suggests a mercury oxide adlayer beginning to form at the interface (Tostmann *et al.*, 1999; Downs & Hall-Wallace, 2003; Gražulis *et al.*, 2009, 2012), most likely a result of oxygen contamination due to a faulty sample cell seal. The inset in Fig. 4 shows the measured incident angle α_i in dependence of the vertical sample translation z_s (blue circles, measured on the second sample). A fit of equation (1) to the data for $\alpha_i + \alpha_f > 1^\circ$ is shown in black. The fit yields Λ_c = (3.12±0.05) mm, 62.5% larger than the value for a semi-infinite mercury drop. The larger Λ_c as well as the notable deviations in α_i from equation (1) are most likely a result of the deviation of the surface shape from that of the semi-infinite case due to confinement by the sample cell. However, this does not affect the extraction of the reflectivity curve.

Micro-beam XRR curves were collected at all interfaces around the critical angle. In this range in particular, rapid changes in $R(q_z)$ occur, providing a stringent test of this approach. The XRR curves obtained from the mercury samples are shown in Fig. 5(*a*) as red squares and green triangles (mercury/vapour) and blue circles (mercury/electrolyte). The solid lines indicate the theoretical Fresnel reflectivity including absorption effects. For both samples, the observed critical q_z value q_c matches the theoretical values very well [$q_c = 0.065$ $Å^{-1}$ (Henke *et al.*, 1993), see Fig. 5(*a*) inset]. To avoid damaging the detector, the mercury/electrolyte curve and the first part of the mercury/vapour curve (red squares) were recorded with the incident-beam intensity of 3×10^{11} photons s^{-1} (Seeck *et al.*, 2012) attenuated by a factor of 10^5 and 10^4, respectively. The maximum q_z value of the mercury/electrolyte curve is therefore limited to 0.12 $Å^{-1}$ or $1.8q_c$ by the minimum count rate of one photon per exposure over the 1 s counting time (indicated by the dashed blue line). This q_z range is comparable with that reported by Bosio *et al.* (1989). For the second part of the mercury/vapour curve (green triangles), the attenuation was reduced to a factor of ten, thus extending the accessible q_z range to 0.24 $Å^{-1}$ or $3.7q_c$. For $q_z > 0.2$ $Å^{-1}$, the curve shows deviations from the Fresnel curve, most likely due to oxidation of the sample beginning to occur.

Another way to overcome the limitation of the q_z range is to increase the exposure time. Fig. 5(*b*) shows the XRR curves of the water/vapour interface with total exposure times of 1 s (red circles), 10 s (green squares) and 100 s (blue triangles). As before, the horizontal dashed lines indicate the minimum absolute count rate of one photon per pixel over the exposure period. While this threshold decreases with increasing exposure time, the maximum q_z value increases from 0.06 $Å^{-1}$ for 1 s exposure time to 0.18 $Å^{-1}$ for an exposure time of 100 s.

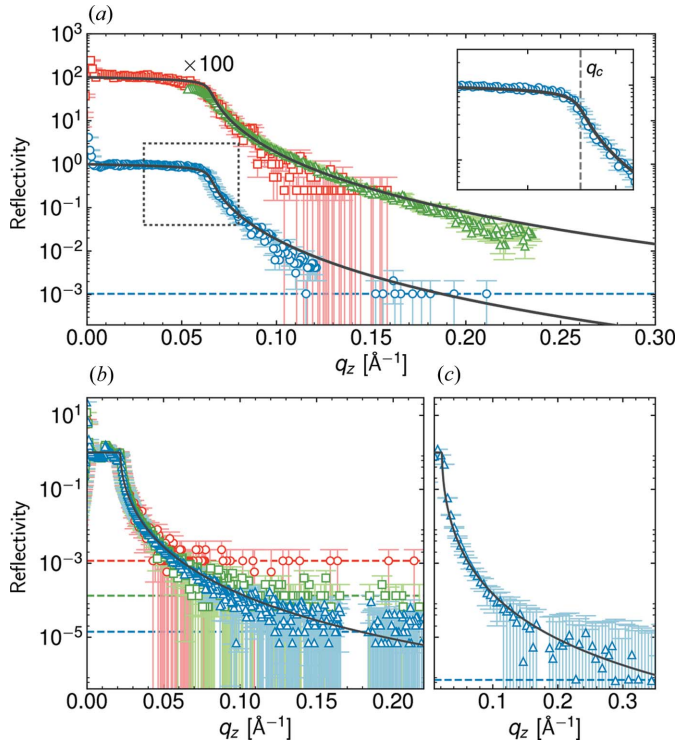

Figure 5
(*a*) XRR curves recorded with the micro-beam method: mercury/vapour interface measured in two parts with 1 s exposure time each (red squares and green triangles, 100 µm beam) and mercury/electrolyte interface (blue circles, 20 µm beam, 1 s total exposure time). The solid black lines denote the Fresnel reflectivity for these interfaces. The dashed horizontal line marks the value corresponding to a total count of one photon. Data for mercury/vapour are offset by a factor of 100. Inset: region close to the critical angle of the Hg reflectivity. (*b*) XRR curves of the water/vapour interface recorded with 1 s (red circles), 10 s (green squares) and 100 s (blue triangles) integration time. Dashed lines indicate the level equivalent to a total flux of one photon. The Fresnel reflectivity is shown as a solid black line. (*c*) Water/vapour reflectivity measured in 100 s. The raw data were binned to extend the accessible q_z range from 0.18 to 0.35 $Å^{-1}$ (blue triangles).

The accessible q_z range can be extended further by binning of the raw data. Considering the high resolution of the raw data (approximately 0.0005 $Å^{-1}$), the reduction of resolution from averaging over ten points does not impose serious limitations on the usability of the data. The effect of binning is shown in Fig. 5(*c*), in which the water/vapour XRR curve recorded with 100 s exposure time [as shown in Fig. 5(*b*) as blue triangles] was binned over q_z intervals of 0.005 $Å^{-1}$ width. In comparison with the original data, the lowest accessible intensity is more than a factor of ten lower (dashed blue line), thus extending the accessible q_z range from 0.18 to 0.35 $Å^{-1}$ or approximately $5q_c$.

5. Conclusion and outlook

We successfully implemented a method that enables the measurement of liquid–liquid and liquid–vapour XRR curves using a fixed, horizontal source beam, a vertical translation stage and a two-dimensional detector. Using a nanometre beam, it is possible to probe one single angle at a time

analogous to classical XRR techniques while maintaining the accessible q_z range. Alternatively, a larger beam (of the order of micrometres) can be used that is reflected into a wider angular range, enabling parallel measurements of a larger range of an XRR curve up to $5\alpha_c$. The feasibility of both modes was demonstrated by recording the XRR curves of the mercury/vapour, mercury/electrolyte and water/vapour interfaces. The obtained XRR curves match the results known from previous studies by conventional XRR techniques.

The presented method is experimentally simple and does not require a specific liquid diffractometer, but requires trade-offs regarding accessible q_z range, signal-to-noise ratio and most notably q_z resolution. Which of these limitations apply depends on the employed measurement mode. As low divergence is crucial to the feasibility of the method, its application is limited to high-brilliance X-ray sources such as third-generation synchrotrons and FELs.

XRR measurement on drop samples therefore will not render specialized diffractometers obsolete. It will, however, enable studies of liquid interfaces at sources lacking liquid diffractometers, especially ultra-fast XRR measurements *via* pump–probe techniques at FELs. A future combination of the method with drop shape analysis methods (Hoorfar & Neumann, 2011) should allow independent determination of $z_s(x)$, which can be used for improving the quality of the extracted data. In addition, the method may be extended to more complex experiments, for example the study of free falling or levitated drops.

Acknowledgements

We thank the beamline staff of P08 at DESY and ID13 at ESRF for their kind support.

Funding information

Funding for this research was provided by: Bundesministerium für Bildung und Forschung (grant No. 05K10FK2; grant No. 05K13FK2; grant No. 05K16FK1); Deutsche Forschungsgemeinschaft (grant No. MA 16/18); European Synchrotron Radiation Facility; Deutsches Elektronen-Synchrotron.

References

Adamson, A. W. & Gast, A. P. (1997). *Physical Chemistry of Surfaces.* New York: Wiley.
Als-Nielsen, J. & McMorrow, D. (2011). *Elements of Modern X-ray Physics*, 2nd ed. New York: Wiley.
Als-Nielsen, J. & Pershan, P. S. (1983). *Nucl. Instrum. Methods Phys. Res.* **208**, 545–548.
Bosio, L., Cortes, R., Denoziere, M. & Folcher, G. (1989). *J. Phys. Colloq.* **50**, C7-23–C7-27.
Braslau, A., Pershan, P. S., Swislow, G., Ocko, B. M. & Als-Nielsen, J. (1988). *Phys. Rev. A*, **38**, 2457.
Briscoe, W. H., Speranza, F., Li, P., Konovalov, O., Bouchenoire, L., van Stam, J., Klein, J., Jacobs, R. M. J. & Thomas, R. K. (2012). *Soft Matter*, **8**, 5055.
Dean, J. A. & Lange, N. A. (1999). *Lange's Handbook of Chemistry*, 15th ed. New York: McGraw-Hill.
Dimasi, E. & Tostmann, H. (1999). *Synchrotron Radiat. News*, **12**, 41–46.
Downs, R. T. (2003). *Am. Mineral.* **88**, 556–566.
Gennes, P. G. de, Brochard-Wyart, F. & Quere, D. (2004). *Capillarity and Wetting Phenomena: Drops, Bubbles, Pearls, Waves.* Berlin: Springer.
Gražulis, S., Chateigner, D., Downs, R. T., Yokochi, A. F. T., Quirós, M., Lutterotti, L., Manakova, E., Butkus, J., Moeck, P. & Le Bail, A. (2009). *J. Appl. Cryst.* **42**, 726–729.
Gražulis, S., Daškevič, A., Merkys, A., Chateigner, D., Lutterotti, L., Quirós, M., Serebryanaya, N. R., Moeck, P., Downs, R. T. & Le Bail, A. (2012). *Nucleic Acids Res.* **40**, D420–D427.
Henke, B. L., Gullikson, E. M. & Davis, J. C. (1993). *At. Data Nucl. Data Tables*, **54**, 181–342.
Honkimäki, V., Reichert, H., Okasinski, J. S. & Dosch, H. (2006). *J. Synchrotron Rad.* **13**, 426–431.
Hoorfar, M. & Neumann, A. W. (2011). In *Applied Surface Thermodynamics*, 2nd ed, edited by A. W. Neumann, R. David & Y. Zuo, ch. 3. Boca Raton: CRC Press.
Kawamoto, E. H., Lee, S., Pershan, P. S., Deutsch, M., Maskil, N. & Ocko, B. M. (1993). *Phys. Rev. B*, **47**, 6847–6850.
Magnussen, O. M., Ocko, B. M., Regan, M. J., Penanen, K., Pershan, P. S. & Deutsch, M. (1995). *Phys. Rev. Lett.* **74**, 4444–4447.
Metzger, T. H., Luidl, C., Pietsch, U. & Vierl, U. (1994). *Nucl. Instrum. Methods Phys. Res. A*, **350**, 398–405.
Murphy, B. M., Greve, M., Runge, B., Koops, C. T., Elsen, A., Stettner, J., Seeck, O. H. & Magnussen, O. M. (2014). *J. Synchrotron Rad.* **21**, 45–56.
Naudon, A., Chihab, J., Goudeau, P. & Mimault, J. (1989). *J. Appl. Cryst.* **22**, 460–464.
Pershan, P. S. & Schlossman, M. (2012). *Liquid Surfaces and Interfaces: Synchrotron X-ray Methods.* Cambridge University Press.
Pietsch, U., Grenzer, J., Geue, T., Neissendorfer, F., Brezsesinski, G., Symietz, C., Möhwald, H. & Gudat, W. (2001). *Nucl. Instrum. Methods Phys. Res. A*, **467–468**, 1077–1080.
Regan, M. J., Tostmann, H., Pershan, P. S., Magnussen, O. M., DiMasi, E., Ocko, B. M. & Deutsch, M. (1997). *Phys. Rev. B*, **55**, 10786–10790.
Riekel, C., Burghammer, M. & Davies, R. (2010). *Mater. Sci. Eng.* **14**, 012013.
Runge, B., Festersen, S., Koops, C. T., Elsen, A., Deutsch, M., Ocko, B. M., Seeck, O. H., Murphy, B. M. & Magnussen, O. M. (2016). *Phys. Rev. B*, **93**, 165408.
Schlossman, M. L., Synal, D., Guan, Y., Meron, M., Shea-McCarthy, G., Huang, Z., Acero, A., Williams, S. M., Rice, S. A. & Viccaro, P. J. (1997). *Rev. Sci. Instrum.* **68**, 4372–4384.
Seeck, O. H., Deiter, C., Pflaum, K., Bertam, F., Beerlink, A., Franz, H., Horbach, J., Schulte-Schrepping, H., Murphy, B. M., Greve, M. & Magnussen, O. (2012). *J. Synchrotron Rad.* **19**, 30–38.
Seeck, O. H. & Murphy, B. (2015). *X-ray Diffraction: Modern Experimental Techniques*. Singapore: Pan Stanford Publishing.
Shpyrko, O., Huber, P., Grigoriev, A., Pershan, P., Ocko, B., Tostmann, H. & Deutsch, M. (2003). *Phys. Rev. B*, **67**, 115405.
Tostmann, H., DiMasi, E., Ocko, B. M., Deutsch, M. & Pershan, P. S. (1999). *J. Non-Cryst. Solids*, **250–252**, 182–190.
Yano, Y. F., Uruga, T., Tanida, H., Toyokawa, H., Terada, Y., Takagaki, M. & Yamada, H. (2009). *Eur. Phys. J. Spec. Top.* **167**, 101–105.